H. Guo

Department of Mechanical and Aerospace
Engineering,
Missouri University of Science and Technology,
1870 Miner Circle,
Rolla, MO 65409

J. Hu

Department of Mechanical Engineering,
University of Bridgeport,
Bridgeport, CT 06604
e-mail: jjhu@bridgeport.edu

H. L. Tsai

Department of Mechanical and Aerospace
Engineering,
Missouri University of Science and Technology,
1870 Miner Circle,
Rolla, MO 65409

Three-Dimensional Modeling of Gas Metal Arc Welding of Aluminum Alloys

A three-dimensional mathematical model and numerical techniques were developed for simulating a moving gas metal arc welding process. The model is used to calculate the transient distributions of temperature and velocity in the weld pool and the dynamic shape of the weld pool for aluminum alloy 6005-T4. Corresponding experiments were conducted and in good agreement with modeling predictions. The existence of a commonly observed cold-weld at the beginning of the weld, ripples at the surface of the weld bead, and crater at the end of the weld were all predicted. The measured microhardness around the weld bead was consistent with the predicted peak temperature and other metallurgical characterizations in the heat-affected zone. [DOI: 10.1115/1.4001479]

Keywords: gas metal arc welding, aluminum, ripples, weld

1 Introduction

Gas metal arc welding (GMAW) is one of the most popular welding methods in the industry. It is an arc welding process, which uses a metal wire as a combined electrode and filler metal in a plasma arc and inert shielding gas. GMAW has some advantages over other welding methods, such as high productivity, better penetration, no need for flux, little spatter, and ability to weld in all positions. In the auto-industry, due to the demands for a lower environmental impact through improved fuel efficiency, weight reduction, and load capacity, aluminum is being more widely used. A typical weld bead in GMAW of aluminum alloys, as shown in Fig. 1, can be divided into three zones. At the beginning of the weld, the base metal is heated up from room temperature, electrode material starts to drop onto the welding coupon, and the weld bead begins to form. In this zone, the welding process is not in a quasisteady state and a cold-weld is formed. The weld pool temperature, fluid flow, and weld bead shape vary constantly. At the middle of the weld, the welding process is at a quasisteady state. When the welding comes to an end, the arc is terminated and there is neither energy nor material transfer into the weld pool. The molten pool solidifies and forms a crater-shaped weld end. It can be clearly seen in Fig. 1 that ripples are formed at the surface of the weld bead. In this paper, the modeling of the normal weld in the middle of the welding process will be reported and the other two zones are covered in other papers.

To get a better understanding of the GMAW process of aluminum alloys, both experimental and theoretical studies should be carried out. Many experimental investigations have been conducted on the GMAW process [1–8]. GMAW is a very complicated process involving many coupled parameters such as welding current, voltage, welding speed, electrode feed speed, base metal chemical composition, electrode material, electrode size, and shielding gas. In addition, because welding is a transient process at high temperatures, it is hard to use experimental methods alone to understand the transport phenomena involved. Mathematical modeling provides a convenient way to obtain insightful information.

Many theoretical models have been proposed on the simulation of a gas metal arc welding process. Ushio and Wu [9] proposed a model to calculate the three-dimensional heat and fluid flow in a moving gas metal arc weld pool. A boundary-fitted nonorthogonal coordinate system was adopted and it was found that the size and profile of the weld pool are strongly influenced by the volume of the molten wire, impact of droplets, and heat content of the droplets. Park and Rhee [10] reported that the kinetic energy of the transferring droplets produces a depression on the weld pool surface. According to the computational investigations by Davies et al. [11], the impinging droplet momentum dominates the flow pattern and overrides any surface tension effects at a relatively high current. While a flat weld pool surface is assumed in the 3D GMAW model of Jaidi and Dutta [12], the surface deformation caused by the droplet impingement and weld pool dynamics is calculated by Wang and Tsai [13], Hu and Tsai [14], and Hu et al. [15]. All those research efforts were only focused on the GMAW of steels. There is hardly any three-dimensional mathematical modeling on the GMAW of aluminum alloys. However, the welding behavior of aluminum alloys differs significantly from steel with physical properties [16], such as high thermal conductivity, lower melting point, high coefficient of thermal expansion, high solidification shrinkage, oxide formation at the surface, etc.

The objectives of this project are to conduct numerical simulation and experimental validation on the GMAW of aluminum alloys. The three-dimensional fluid flow and heat transfer were calculated when droplets carrying mass, momentum, and thermal energy impinged onto the weld pool. The transient deformed weld pool surface was handled by the volume of fluid (VOF) technique [17], and the fusion and solidification in the liquid region, the mushy zone, and the solid region were handled by the continuum formulation [18]. Bead-on-plate experiments were performed, and the welded samples were characterized to determine the microhardness in the weld bead.

2 Mathematical Model

A sketch of a moving GMAW for a bead-on-plate welding is shown in Fig. 2. The base metal is aluminum alloy 6005-T4. The three-dimensional *x-y-z* coordinate system is fixed to the base metal. The arc is moving in the positive *x* direction, and droplets impinge onto the base metal in the negative *z* direction while moving at the same velocity along the *x* direction as the arc. Since
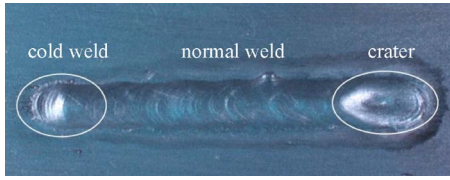
Copyright © 2010 by ASME

Fig. 1 A typical weld bead of GMAW of aluminum alloys

the welding process is symmetrical with respect to the x-z plane, only half of the domain in the y direction is included in the calculation.

2.1 Governing Equations. The differential equations governing the conservation of mass, momentum, and energy based on continuum formulation given by Diao and Tsai [18] were modified and employed in the study, and they are given as follows.

(1) Continuity,

$$\frac{\partial \rho}{\partial t} + \nabla \cdot (\rho \vec{V}) = 0 \tag{1}$$

where t is the time, ρ is the density, and $\vec{V}$ is the velocity vector.

(2) Momentum,

$$\frac{\partial}{\partial t}(\rho u) + \nabla \cdot (\rho \vec{V} u) = \nabla \cdot \left(\mu_l \frac{\rho}{\rho_l} \nabla u \right) - \frac{\partial p}{\partial x} - \frac{\mu_l}{K}\frac{\rho}{\rho_l}(u - u_s)$$
$$- \frac{C\rho^2}{K^{1/2}\rho_l}|u - u_s|(u - u_s)$$
$$- \nabla \cdot (\rho f_s f_l \vec{V}_r u_r) + \vec{J} \times \vec{B}|_x \tag{2}$$

$$\frac{\partial}{\partial t}(\rho v) + \nabla \cdot (\rho \vec{V} v) = \nabla \cdot \left(\mu_l \frac{\rho}{\rho_l} \nabla v \right) - \frac{\partial p}{\partial y} - \frac{\mu_l}{K}\frac{\rho}{\rho_l}(v - v_s)$$
$$- \frac{C\rho^2}{K^{1/2}\rho_l}|v - v_s|(v - v_s)$$
$$- \nabla \cdot (\rho f_s f_l \vec{V}_r v_r) + \vec{J} \times \vec{B}|_y \tag{3}$$

$$\frac{\partial}{\partial t}(\rho w) + \nabla \cdot (\rho \vec{V} w) = \nabla \cdot \left(\mu_l \frac{\rho}{\rho_l} \nabla w \right) - \frac{\partial p}{\partial z} - \frac{\mu_l}{K}\frac{\rho}{\rho_l}(w - w_s)$$
$$- \frac{C\rho^2}{K^{1/2}\rho_l}|w - w_s|(w - w_s)$$
$$- \nabla \cdot (\rho f_s f_l \vec{V}_r w_r) + \rho g + \rho g (\beta_T (T - T_0) + \beta_s (f_l^\alpha - f_{l,0}^\alpha)) + \vec{J} \times \vec{B}|_z + F_{\mathrm{drag}} \tag{4}$$

where u, v, and w are the velocities in the x, y, and z directions, respectively, and $\vec{V}_r = \vec{V}_l - \vec{V}_s$ is the relative velocity vector between the liquid phase and the solid phase. The subscripts s and l refer to the solid and liquid phases, respectively; p is the pressure; μ is the dynamic viscosity; f is the mass fraction; K is the permeability, a measure of the ease with which fluids pass through the porous mushy zone; C is the inertial coefficient; β_T is the thermal expansion coefficient; g is the gravitational acceleration; T is the temperature; $\vec{B}$ is the magnetic induction vector; $\vec{J}$ is the current density vector; and the subscript 0 represents the initial condition.

(3) Energy,

$$\frac{\partial}{\partial t}(\rho h) + \nabla \cdot (\rho \vec{V} h) = \nabla \cdot \left(\frac{k}{c_s} \nabla h \right) + \nabla \cdot \left(\frac{k}{c_s} \nabla (h_s - h) \right)$$
$$- \nabla \cdot (\rho (\vec{V} - \vec{V}_s)(h_l - h)) \tag{5}$$

where h is the enthalpy, k is the thermal conductivity, and c is the specific heat.

The detailed descriptions of the terms in Eqs. (1)–(5) can be found in Ref. [18], and will not be repeated here. The solid/liquid phase-change is handled by the continuum formulation [18]. The third, fourth, and fifth terms in the right-hand side of Eqs. (2)–(4) vanish at the solid region because of $u = u_s = v = v_s = w = w_s = 0$ and $f_l = 0$ for the solid. In the liquid region, since K goes to infinity, all these terms also vanish [18]. Those terms are only effective for the mushy zone where $0 < f_l < 1$ and $0 < f_s < 1$. Therefore, the liquid region, mushy zone, and solid region can be handled by the same equations. During the fusion and solidification process, latent heat is absorbed or released in the mushy zone. By the use of enthalpy in Eq. (5), conduction in the solid region, conduction and convec-
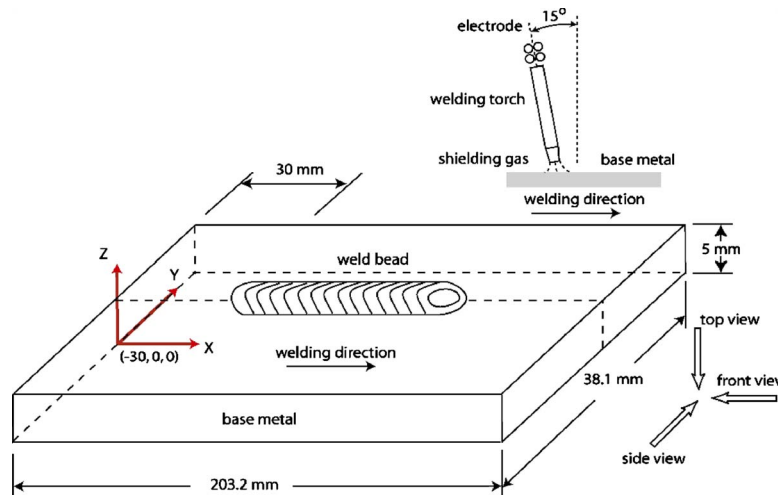

Fig. 2 Experimental setup and simulation domain of a GMAW system

tion in the liquid region and mushy zone, the absorption, and release of latent heat are all handled in the same equation.

2.2 Tracking of Free Surfaces. The fluid configuration is defined by a volume of fluid function [17] $F(x,y,z,t)$, which represents the volume of liquid metal per unit volume and satisfies the following conservation equation:

$$\frac{dF}{dt} = \frac{\partial F}{\partial t} + (\vec{V} \cdot \nabla)F = 0 \tag{6}$$

When averaged over the cells of a computing mesh, the average value of F in a cell is equal to the fractional volume of the cell occupied by fluid. A unit value of F corresponds to a cell full of fluid, whereas a zero value indicates a cell with no fluid. Cells with F values between 0 and 1 are partially filled with fluid and identified as surface cells. Gradients of F determine the mean local surface normal, and, together with F values, allow the construction of an approximate interface.

2.3 Boundary Conditions. The boundary conditions for the previous equations (Eqs. (1)–(5)) are given below.

2.3.1 Normal to the Local Free Surface. For cells containing a free surface, that is, cells that contain fluid but have one or more empty neighbors, the following pressure conditions must be satisfied [14]:

$$p = p_v + \gamma \kappa \tag{7}$$

where p is the pressure at the free surface in a directional normal to the local free surface and p_v is the plasma arc pressure, which is assumed to have a radial distribution in the following form [13]:

$$p_v = P_{\max} \exp\left(-\frac{r^2}{2\sigma_p^2}\right) \tag{8}$$

where $P_{\max}$ is the maximum arc pressure at the arc center, which is calculated from welding current [13], r is the distance from the arc center, and σ_p is the arc pressure distribution parameter [13]. κ in Eq. (7) is the free surface curvature given by

$$\kappa = -\left[\nabla \cdot \left(\frac{\vec{n}}{|\vec{n}|}\right)\right] = \frac{1}{|\vec{n}|}\left[\left(\frac{\vec{n}}{|\vec{n}|} \cdot \nabla\right)|\vec{n}| - (\nabla \cdot \vec{n})\right] \tag{9}$$

where $\vec{n}$ is the normal vector to the local surface, which is the gradient of VOF function

$$\vec{n} = \nabla F \tag{10}$$

2.3.2 Tangential to the Local Free Surface. The Marangoni shear stress at the free surface in a direction tangential to the local free surface is given by

$$\tau_{\vec{s}} = \mu_l \frac{\partial(\vec{V} \cdot \vec{s})}{\partial \vec{n}} = \frac{\partial \gamma}{\partial T}\frac{\partial T}{\partial \vec{s}} \tag{11}$$

where $\vec{s}$ is the local surface tangential vector. Since there are no surface tension coefficient data available for 6005-T4, the property of pure aluminum was used instead. For pure aluminum, surface tension coefficient γ is a function of temperature [19].

$$\gamma = 868 - 0.152(T - T_l) \tag{12}$$

where T is the temperature and T_l is the melting temperature of aluminum.

2.3.3 Top Surface. At the arc center, in addition to droplet impingement, arc heat flux is also impacting on the base metal. Since the arc heat flux is relatively concentrated, it is assumed that the heat flux is perpendicular to the base metal (i.e., neglecting the inclination of current and heat flux). Therefore the temperature boundary conditions at the top surface of the base metal are

$$k\frac{\partial T}{\partial z} = \frac{\eta(1-\eta_d)Iu_w}{2\pi\sigma_q^2}\exp\left(-\frac{r^2}{2\sigma_q^2}\right) - q_{\text{conv}} - q_{\text{radi}} - q_{\text{evap}} \tag{13}$$

where I is the welding current, η is the arc thermal efficiency, η_d is the ratio of droplet thermal energy to the total arc energy, u_w is the arc voltage, and σ_q is the arc heat flux distribution parameter [13]. The heat loss due to convection, radiation, and evaporation can be written as

$$q_{\text{conv}} = h_c(T - T_\infty), \quad q_{\text{radi}} = \sigma\varepsilon(T^4 - T_\infty^4), \quad q_{\text{evap}} = WH_v \tag{14}$$

where h_c is the convective heat transfer coefficient [13], T_∞ is the room temperature, which is 293 K in this case, σ is Stephan–Boltzmann constant, ε is the surface radiation emissivity, H_v is the latent heat for the liquid-vapor phase-change, and W is the melt mass evaporation rate [20].

2.3.4 Symmetrical y=0 Plane.

$$\frac{\partial T}{\partial y} = 0, \quad \frac{\partial u}{\partial y} = 0, \quad v = 0, \quad \frac{\partial w}{\partial y} = 0, \quad \frac{\partial f^\alpha}{\partial y} = 0 \tag{15}$$

2.3.5 Other Surfaces.

$$-k\frac{\partial T}{\partial \vec{n}} = q_{\text{conv}}, \quad u = 0, \quad v = 0, \quad w = 0 \tag{16}$$

2.4 Electromagnetic Force. In Eqs. (2)–(4), there are three terms caused by the electromagnetic force. In order to solve these three terms, $\vec{J} \times \vec{B}$ should be calculated first before the calculation of velocity. Assuming the electric field is a quasi-steady-state and the electrical conductivity is constant, the scalar electric potential ϕ satisfies the following Maxwell equation [13] in the local r-z coordinate system:

$$\nabla^2\phi = \frac{1}{r}\frac{\partial}{\partial r}\left(r\frac{\partial\phi}{\partial r}\right) + \frac{\partial^2\phi}{\partial z^2} = 0 \tag{17}$$

The required boundary conditions for the solution of Eq. (17) are

$$-\sigma_e\frac{\partial\phi}{\partial z} = \frac{I}{2\pi\sigma_c^2} \times \exp\left(-\frac{r^2}{2\sigma_c^2}\right) \quad \text{at the top free surface} \tag{18}$$

$$\frac{\partial\phi}{\partial z} = 0 \quad \text{at} \quad z = 0 \tag{19}$$

$$\frac{\partial\phi}{\partial r} = 0 \quad \text{at} \quad r = 0 \tag{20}$$

$$\phi = 0 \quad \text{at} \quad r = 10\sigma_c \tag{21}$$

where σ_e is the electrical conductivity and σ_c is the arc current distribution parameter [13]. The current density in the r and z directions can be calculated via

$$J_r = -\sigma_e\frac{\partial\phi}{\partial r}, \quad J_z = -\sigma_e\frac{\partial\phi}{\partial z} \tag{22}$$

The self-induced azimuthal magnetic field is derived from Ampere's law [13]

$$B_0 = \frac{\mu_0}{r}\int_0^r J_z r dr \tag{23}$$

where μ_0 is the magnetic permeability in free space. Finally, the three components of electromagnetic force in Eqs. (2)–(4) are calculated via the following equations [13]:

$$\vec{J} \times \vec{B}\big|_x = -B_\theta J_z \frac{x-x_a}{r}, \quad \vec{J} \times \vec{B}\big|_y = -B_\theta J_z \frac{y}{r}, \quad \vec{J} \times \vec{B}\big|_z = B_\theta J_r$$

$$(24)$$

2.5 Numerical Considerations. The governing equations were solved iteratively at each time step using the finite volume method [21]. At each time step, the continuity and momentum equations were solved iteratively with a two-step projection method involving the time discretization of the momentum equations to get the velocity and pressure distributions [15]. Then the energy equation was solved explicitly to obtain the enthalpy and temperature field. The species equation was solved in a similar way. This process was repeated for each iteration step. Iteration within a time step was terminated when the solutions of velocity, pressure, temperature, and species distributions converged. Then the VOF function equation was solved to obtain the new free surface and liquid pool domain. The temperature-dependent material properties were updated. The time step was then advanced and the above procedure was repeated until the desired time was reached.

Since the governing equations are valid for the entire computational domain including the liquid phase, the solid phase, and the mushy zone, there is no need to track the shape and extent of each phase. Therefore, a fixed grid system was used in the calculation with refined grid cells in the weld pool zone to improve accuracy. Due to the symmetry of the x-z plane of the domain, a grid system of $408 \times 66 \times 56$ points was used for the half computational domain to save computational time. The finer grids concentrating on and around the weld pool move with the weld pool as the welding proceeds. Time-step length varied during the calculation to ensure the convergence and save computational time. The average time step is around 2×10^{-5} s. Extensive tests using different grid sizes and time-step sizes have been conducted to assure consistent results. The final grid and time-step sizes used in the present study can be considered as the compromised values between computational time and accuracy.

The computation was performed on the Dell Precision 650® workstations with 3.2 GHz Pentium® 4 processors. It took about 71 h of CPU time to simulate 1.4 s of real-time welding.

3 Experiments

The experimental setup is shown in Fig. 2. Bead-on-plate welds were made on aluminum alloy 6005-T4 plates $203.2 \times 38.1 \times 5$ mm³ in dimension, which were extruded by Hydro Raufoss Automotive. Alloying elements in 6005-T4 are 0.6–0.9 wt % Si, 0.4–0.6 wt % Mg, <0.35 wt % Fe, <0.1 wt % Cu, <0.1 wt % Mn, <0.1 wt % Cr, <0.1 wt % Zn, and <0.1 wt % Ti [22]. Every weld coupon was chemically cleaned and degreased. The electrode material was 4043 produced by Alcoa and the major alloying element is 5.2 wt % of silicon. The diameter of the electrode wire was 1.6 mm in all experiments. The welding machine was a Lincoln PowerWave 455® programmable waveform controlled welding machine made by Lincoln Electric, Cleveland, OH. The weld torch was fixed onto a small cart on a rail. Argon was used as the protecting gas, the flow rate of which was 40 cubic feet per hour (7.87 cm³/s). To provide an adequate protection of the weld pool, a welding gun leading angle of 15 deg was used in the experiments. The weld bead was made under constant current mode of the welding machine with direct current electrode positive (DCEP) connection at the center of the plate along the x direction, as shown in Fig. 2. All welds started from 30 mm to the left end of the weld coupon. Before welding, the upper surface of the plate was brushed with a stainless steel brush to remove the oxide layer. Three major parameters could be adjusted during the process: welding current, wire feed speed, and arc/cart travel speed. Arc voltage was automatically set by the welding machine once the other parameters were fixed.

The experiments were closely monitored during the process and the welding parameters were recorded to be input into the mathematical model. This was achieved by connecting the port on the PowerWave455® front panel to the serial port of a computer and using WaveDesigner® software from Lincoln Electric. The welding parameters, such as arc current, voltage, and welding time, were stored in the computer and used as input in the mathematical model.

Welded samples were sectioned, grinded, polished, and then etched for metallurgical characterizations. Sectioning was performed along cross-sectional and longitudinal directions of the weld coupon on a Leco CM-15® cut-off machine. The sample grinding and polishing were performed on a Leco Spectrum System2000® grinder/polisher. The polished samples were then etched by Tucker's reagent and Keller's reagent [23] for macroscopy and microscopy analyses, respectively. Macroscopy analysis was performed under stereoscopes and optical microscopes. An image acquisition system including a digital camera and a computer was used to capture and store the images. The weld penetration, width, and reinforcement were measured. Knoop hardness measurements were performed on the cross sections of weld samples using a load of 100 g.

4 Results and Discussion

The formation of the weld bead for a GMAW of 6005-T4 aluminum alloy was calculated. The fluid flow pattern, temperature distribution, and the weld bead shape were obtained. The welding current is 183 A, voltage is 23.5 V, wire feed speed is 69.8 mm/s, and welding speed is 14.8 mm/s. Table 1 lists the other welding conditions and simulation parameters. The simulation parameters are based on the welding conditions and the results from our previous studies on droplet generation and transfer [14,15,24–26]. Simulation is started when the welding arc is ignited at $x=0$, 30 mm to the left edge of the plate. To simulate a realistic welding process where the weld torch has a 15 deg lead angle and to account for the moving speed of the welding arc, the droplet also has a horizontal velocity in the arc moving direction in addition to the vertical velocity.

Figure 3 shows a partial three-dimensional view of the simulated quasisteady welding process. It is observed that a cold-weld at the beginning, a crater at the end, and ripples are formed on the weld bead by the impinging droplets. The temperature, fluid flow, and formation of ripples will be discussed in Secs. 4.1–4.3.

4.1 Side View of the Welding Process. Figures 4–6 show the side views of the welding process showing the weld pool, temperature field, and velocity distribution, respectively. At $t=2.8200$ s, before a new droplet's impingement onto the weld pool, both the previously deposited material and the base metal are melted by the welding arc. The lowest height of the depressed weld pool surface is not right under the arc center, but behind it. For example, at $t=2.8200$ s, the deepest surface point is nearly 2 mm behind the arc center. The deepest penetration occurs slightly behind the lowest weld pool surface point, and also around 2 mm behind the arc center. These phenomena are the results of fluid flow pattern and heat transfer in the weld pool. The fluid in the weld pool flows away from the arc center in two directions: one in the welding direction and the other one in the opposite direction. The fluid flows downward, and, when reaching the bottom of the weld pool at the weld center, part of the fluid flows to the left, then upwards along the solid-liquid boundary and the rest flows upward to the right. It takes some time for the heat to transfer into the base metal and melt the solid material. Hence, the base metal continues to melt even after the arc center has passed by, causing the deepest penetration to occur behind the weld arc center. The isotherms in Fig. 5 clearly show the heat propagation in the base metal, where the deepest point of isotherm of 880 K is to the left of 927 K. Since the solid-liquid boundary is deeper into the base metal where penetration is deeper and the fluid flowing to the left

Table 1 Thermophysical properties and welding conditions used in the model

Property	Symbol	Value (unit)
Specific heat of solid phase	c_s	900[a] (J/kg K)
Specific heat of liquid phase	c_l	900[a] (J/kg K)
Thermal conductivity of solid phase	k_s	167[b] (W/m K)
Thermal conductivity of liquid phase	k_l	167[b] (W/m K)
Density of solid phase	ρ_s	2700[b] (kg/m^3)
Density of liquid phase	ρ_l	2300[b] (kg/m^3)
Coefficient of thermal expansion	β_T	2.34×10^{-5} [b] (/K)
Radiation emissivity	ε	0.4
Dynamic viscosity	μ_l	0.0012[a] (kg/m s)
Heat of fusion	H	3.97×10^5 [a] (J/kg)
Heat of vaporization	H_v	1.08×10^7 [a] (J/kg)
Solidus temperature	T_s	880[b] (K)
Liquidus temperature	T_l	927[b] (K)
Ambient temperature	T_∞	293 (K)
Convective heat transfer coefficient	h_c	80 (W/m^2 s)
Electrical conductivity	σ_e	2.5×10^7 [b] (Ω^{-1} m^{-1})
Welding voltage	u_w	23.5 (V)
Welding current	I	183 (A)
Arc heat flux distribution parameter	σ_q	2.50×10^{-3} (m)
Arc current distribution parameter	σ_c	2.50×10^{-3} (m)
Welding speed	V_a	14.8 (mm s^{-1})
Arc thermal efficiency	η	60%
Welding speed	V_a	14.8 (mm s^{-1})
Arc thermal efficiency	η	60%
Ratio of droplet thermal energy to total arc energy	η_d	20%
Thickness of base metal	H_b	5.0 (mm)
Width of base metal	W_b	38.1 (mm)
Length of base metal	L_b	203.2 (mm)
Initial base metal temperature	T_b	293 (K)
Initial base metal sulfur concentration	f_b^α	100 (ppm)
Electrode wire diameter	d_w	1.60 (mm)
Electrode wire feed speed	V_w	69.8 (cm/s)
Droplet diameter	D_d	1.0 (mm)
Droplet generation frequency	F_d	268 (Hz)
Droplet impinging velocity	V_d	50 cm/s
Initial droplet temperature	T_d	1050 (K)
Initial droplet sulfur concentration	f_d^α	300 (ppm)
Maximum plasma arc pressure	P_{max}	200 (Pa)
Plasma arc pressure distribution parameter	σ_p	5.0×10^{-3} (m)

[a]Property of pure aluminum [19].
[b]Property of 6005 [22].

follows the solid-liquid interface, the molten metal continues to flow downward and leftward until it reaches the deepest penetration position where it begins to flow upward and leftward. Therefore, the lowest weld pool surface point is located behind the weld arc center and near the deepest penetration position. The velocity of fluid decreases as it flows uphill, and when reaching the tail
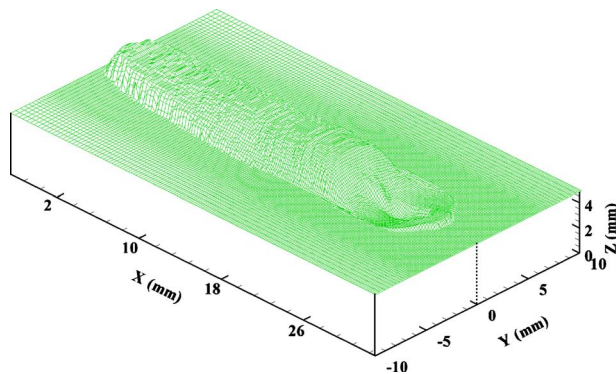

Fig. 3 Partial three-dimensional view of the simulated weld at t=1.8800 s

edge of the weld pool, the fluid solidifies and forms the top surface of the weld bead. A weld pool with a crater-shaped surface is thus formed due to this flow pattern.

The fluid flow pattern is primarily caused by the combined effect of three factors: first, arc pressure, which depresses the free surface; second, surface tension, which drives the fluid flow outwards in this case, according to Eq. (12), the surface tension coefficient decreases as the temperature increases, leading to the outward surface tension force from the high temperature arc center; and third, droplet impingement, which drives the flow downward and outward from the arc center. These three factors maintain the outward flow and keep the weld pool surface profile. Compared with the weld pool formed in the GMAW of steels [15], the thickness of the molten metal layer in the aluminum weld pool is thinner because of the faster solidification, and there is no vortex developed in the weld pool.

4.2 Front View of the Welding Process. Figures 7–9 illustrate the front view of the cross-sectional weld bead and weld pool, temperature field, and velocity distribution at the arc center, respectively. When the droplet impinges onto the weld pool at t=2.8240 s, the top droplet fluid near the axis of symmetry keeps flowing downward, while at the same time the bottom droplet fluid away from the axis of symmetry begins to spread out into the
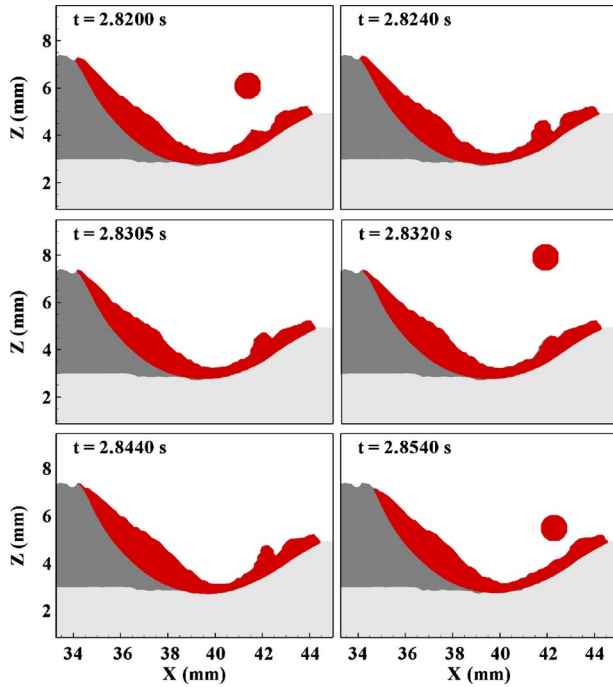
Fig. 4 Side view showing the weld bead shape and weld pool at different times; the region with the darkest color is the weld pool and the second darkest region is the weld bead

Fig. 6 The corresponding velocity distributions of Fig. 4

molten pool in the $\pm Y$ directions. When the downward fluid reaches the weld pool bottom, it spreads into the molten pool along the solid-liquid boundary. The fluid near the impinging droplet flows outwards under the influences of the three aforementioned factors. Further away from the weld pool center, the upward and outward fluid flows become weaker. Near the weld pool edge, the horizontal velocity of the fluid in the Y direction decreases. In the same region, the fluid begins to flow downward under the influence of gravity.

At $t=2.8540$ s, the droplet has mixed with the weld pool completely. The liquid flows downward and outward under the influ-

ence of the three factors mentioned above and thus spreads the melted metal to both sides of the weld. Therefore, the weld pool is depressed to form a crater-shaped surface at the center. At $t=2.8175$ s, a new droplet impinges into the weld pool and the process is repeated for another cycle. Compared with the GMAW of steels [15], the liquid metal is thin, and no vortex is formed on the cross section either.
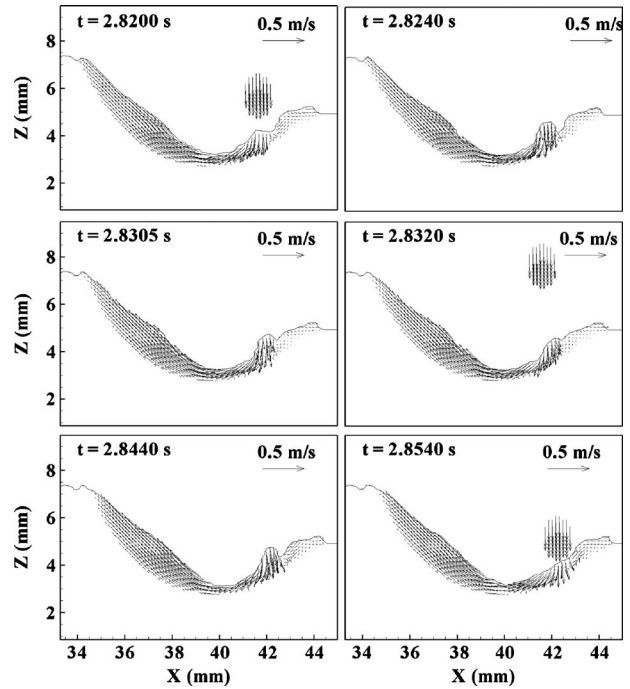
4.3 The Formation of Ripples. As shown in Figs. 3 and 4, ripples formed in the solidified weld bead are very common in the gas metal arc welding process. To determine the formation of weld bead and weld quality, it is very helpful to investigate the
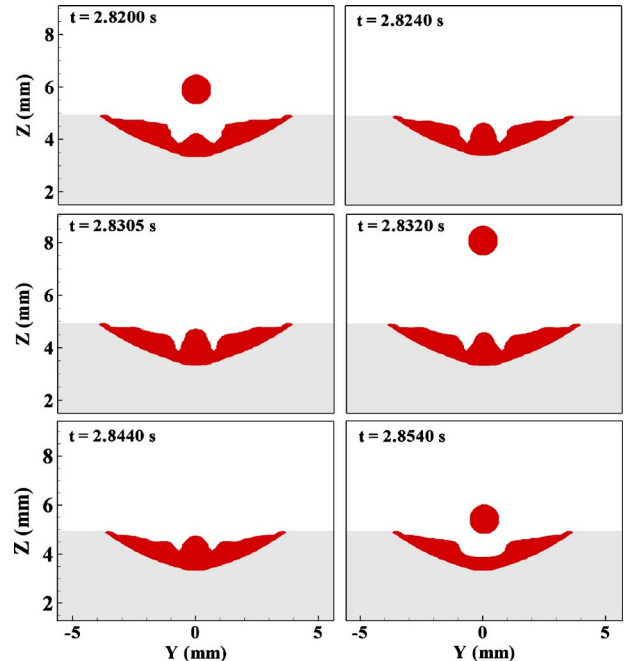

Fig. 5 The corresponding temperature field of Fig. 4

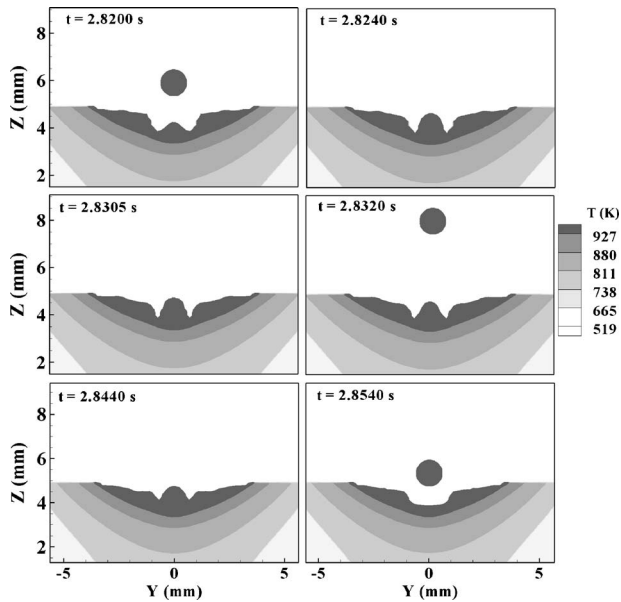**Fig. 7 Front view showing the weld bead shape and weld pool**

Fig. 8 The corresponding temperature field of Fig. 7

mechanism of ripple formation. The previous studies of the formation of ripples in the GMAW of steels [15] found that the waves were formed and propagated toward the rear end of the weld pool. The height level of the fluid upon solidification varied between the "peak" and "valley" of the waves. Thus, ripples were formed in the fully solidified weld bead. Although this mechanism is valid for the GMAW of steels, for gas metal arc welding of aluminum alloys, the weld pool size is much smaller and the thickness of liquid metal is much thinner compared with steels. Therefore, there is no condition for molten metal waves to form and propagate in the weld pool. It is found that the ripple formation is the result of droplet impingement onto the weld pool. The process will be discussed in detail in this section.

The top surface of the weld bead is formed when the fluid solidifies at solidus at the rear end of the weld pool. Since, in the

Fig. 9 The corresponding velocity distributions of Fig. 7

GMAW process, the mushy zone between solidus temperature and liquidus temperature has nearly no flow [15], the height of the liquidus line of 927 K at the tail edge of weld pool is almost the same as the height of the solidified metal next to the weld pool tail edge. The liquidus line can be as high as the ripple peaks.

As shown in Figs. 4–6, at $t=2.8200$ s, at the tail of the weld pool, the liquidus line is at $z=7.1248$ mm, which is at the valley of the last ripple. At $t=2.8240$ s, a new droplet just impinges onto the weld pool. The droplet momentum provides the driving force for the fluid to flow uphill to the rear end of the weld pool. Because of the inertia of the fluid, the left end liquidus line does not rise immediately, which is still at $z=7.1248$ mm. At $t=2.8305$ s, a new droplet falls into the weld pool, providing a new drive force pushing liquid up at the tail edge of the weld pool. The liquidus line at the tail edge begins to rise as a result of the last droplet impingement, increasing to $z=7.2720$ mm. At $t=2.8320$ s, the droplet mixes with the weld pool. The tail edge liquidus line continues to rise as a result of the impingement of the previous droplets, the height of which is $z=7.27998$ mm. The process continues and the subsequent droplets supply a continuous driving force to push the weld pool fluid uphill. The tail edge liquidus line keeps rising until at $t=2.8440$ s, it reaches its peak height of $z=7.3943$ mm. The peak of a new ripple is thus formed. With the increase in fluid level, the gravity force increases gradually. When the fluid level reaches its peak, the gravity force is sufficient to force the fluid to flow downward. Thus, the fluid level begins to fall, leading to the decrease in the tail edge liquidus line. At $t=2.8540$ s, a new ripple is completely formed, the peak of which is at $z=7.3943$ mm. The fluid level decreases to $z=7.1248$ mm, beginning to form a new ripple valley.

From the formation process of a ripple, it is observed that a single droplet does not provide sufficient momentum to drive the fluid flowing upward toward the rear of the weld pool against the hydrostatic force to form a ripple. A series of droplets is needed for the ripple formation. Since there are 154 droplets falling into the weld pool per second in this simulation, from $t=2.8240$ s to $t=2.8440$ s, 3 droplets have impinged onto the weld pool forming the peak of a ripple. The distance between the peaks of the ripple formed during this time period and the previous one is about 0.72 mm.
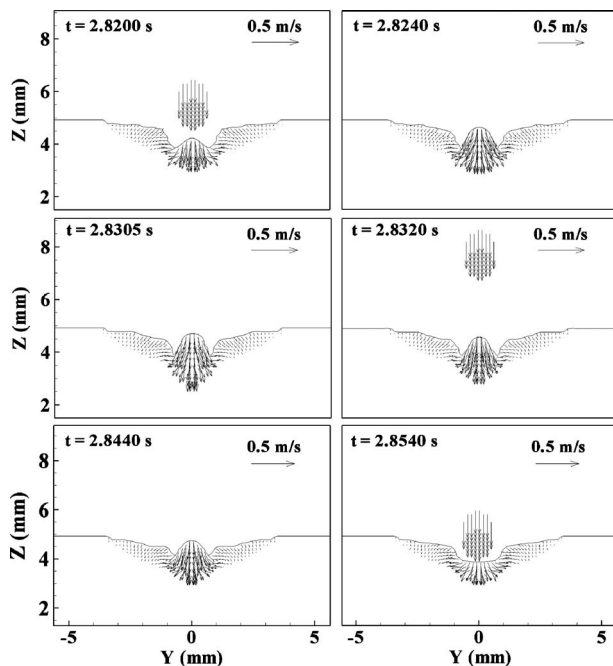
4.4 The Weld Bead Shape. The base metal and the resulting weld are shown in Fig. 10. The black zones in the base metal are Mg_2Si particles [23]. On the cross section near the fusion line, the weld can be divided into three zones: fusion zone (FZ), where the metal was melted and then solidified, partial melted zone (PMZ), where the peak temperature was between the alloy's melting point and eutectic temperature, and heat-affected zone (HAZ), where no melting happened during welding but significant solid-phase transformations took place. The FZ is characterized by columnar dendrites. The dark interdendritic network in the FZ is aluminum-silicon eutectic [23]. The PMZ has a coarse grain structure. In the HAZ near the weld bead, there are fewer Mg_2Si particles than in the base metal since, near the weld bead, the peak temperature is high enough for the particles to dissolve into the aluminum matrix. The cross section of the weld bead at $x=30$ mm is compared with the simulated results in Fig. 11 and Table 2. The zig-zag at the bottom of the simulated weld bead is the result of computational grid. A good agreement between the experimental and calculated results was obtained.

4.5 Microhardness. Knoop microhardness measurements were conducted on the base metal and weld bead. The average hardness is HK 82.17 with a standard deviation of HK 1.56 for the base metal and HK 54.25 with a standard deviation of HK 3.779 for the weld bead. Knoop hardness in the HAZ was measured on the $x=30$ mm cross section along a line 0.4 mm below the top surface of the welding sample (Fig. 12). The results are shown in Fig. 13. It is observed that although the measurement was per-
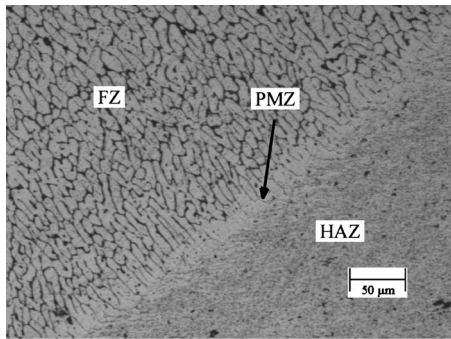
(a)
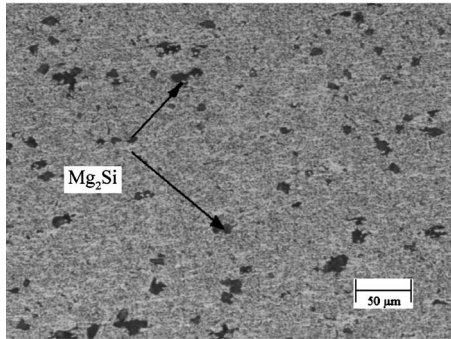
(b)

Fig. 10 Zones near the fusion line at the cross section of the weld: (*a*) zones near the fusion line and (*b*) base metal

formed after 1000 h of natural aging at room temperature, the hardness in the HAZ is still significantly lower than that of the base metal.

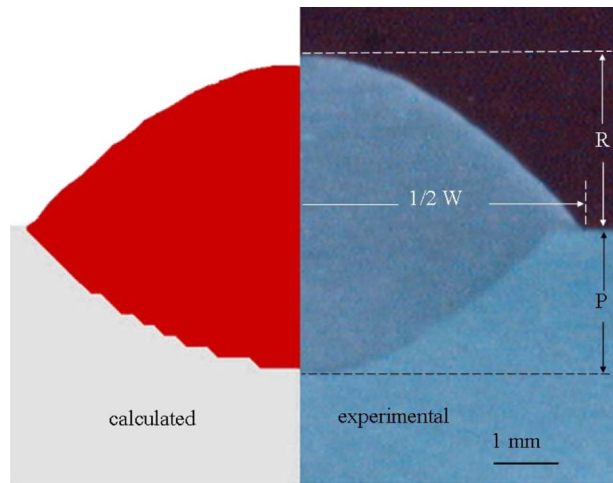The 6005 alloy used in this research is a heat-treatable alumi-

Fig. 11 Comparison of the experimental and calculated results for a cross section at *x*=30 mm

Table 2 Dimensions of cross sections at *x*=30 mm

	Expt.[a]	Simulation
P [b] (mm)	2.15	2.07
W [b] (mm)	7.56	7.65
R [b] (mm)	2.05	2.19

[a]Average values are used for experimental results.
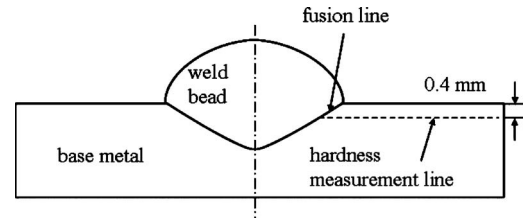[b]P: penetration; W: width; R: reinforcement.

Fig. 12 Knoop hardness measurement positions

num alloy, which gains its strength primarily through the formation of precipitates in the aluminum matrix during heat treatment. Four sequential precipitations may be formed in the alloy during the aging process: the Guinier-Preston (GP) zones, the β'' phase, the β' Mg_2Si phase, and the equilibrium phase β Mg_2Si [19,27,28]. Among the four phases, the β'' phase is the primary strengthening phase in 6xxx series alloys [29]. It is observed from Fig. 13 that for the whole microhardness measurement zone, the peak temperature is above 523 K everywhere. When the temperature is between 523 K and 653 K, the β'' phase coarsens and also transforms to the β' phase, causing lower hardness than that of the base metal. At 653 K, the size of the β'' phase and the amount of the β' phase reach the maximum, and the strength of the metal decreases to a minimum value [28]. This corresponds to the lowest hardness near 5 mm. In the region between 5.76 mm and 3.56 mm to the fusion line, where the temperature is between 653 K and 773 K, dissolution of β'' and β' occurs because the precipitations are held at temperatures higher than the solvus. The dissolution process enriches the solid solution of the aluminum matrix with alloying element Mg [30]. Therefore, this zone may undergo a solution-hardening heat treatment during the heating and cooling of the welding process, which contributes to the rise of local hardness. Thus, a local hardness increase is found at about 3.5 mm. Another contribution to the local hardness rise is that during the postweld natural aging (>3000 h), new precipitates are formed, which can be either GP zones [31] or β'' phases. When the distance to the fusion line is less than 3.56 mm, the temperature is
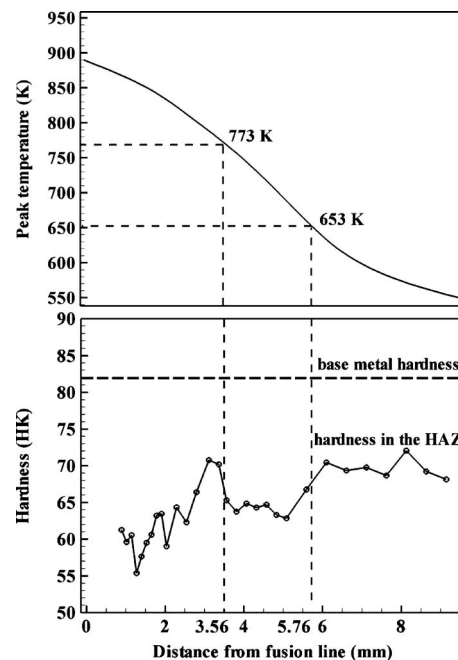

Fig. 13 Knoop hardness measurement results and peak temperature along the hardness measurement line on cross section at *x*=30 mm

higher than 773 K. There are no precipitates in this zone because of the dissolution of the β'' and β' phases [30]. The aluminum matrix is therefore enriched with Mg. The possible reason for the hardness drop may be the diffusion of alloy element Mg between the solid and liquid metals at the interface between the weld pool and solid metal. In the electrode material 4043, the Mg content is far lower than in the base metal [22]. Since areas adjacent to the fusion zone undergo high temperatures during the welding process, the diffusion of Mg may not be negligible, inducing the depletion of Mg in this zone and consequently resulting in the hardness drop near the fusion line.

5 Conclusions

The fluid flow and heat and mass transfer in the weld pool for a moving GMAW of aluminum alloy 6005 were analyzed. Weld pool and weld bead shapes, temperature field, and velocity distribution were obtained for the welding process. Experiments were conducted on the formation of the weld. Metallurgical characterizations together with microhardness measurements were performed. It was found that due to the fast heat dissipation, the weld pool is small compared with the typical GMAW process of steels, and no vortex is formed. The drop impingement, surface tension, and welding arc pressure force the fluid to flow away from the welding arc center. A crater-shaped weld pool is formed as a result. Consecutive droplet impingements are needed for the fluid level at the rear end of the weld pool to vary periodically and form the ripples on the weld bead. Combining the metallurgical analysis and mathematical modeling, it was found that the high peak temperature near the fusion line causes the HAZ softening.

Acknowledgment

Nomenclature

$\vec{B}$ = magnetic induction vector
c = specific heat
C = inertial coefficient
f = mass fraction
F = volume of fluid function
g = gravitational acceleration
h = enthalpy
h_c = convective heat transfer coefficient
H_v = latent heat of vaporization
I = welding current
$\vec{J}$ = current density vector
k = thermal conductivity
K = permeability function
$\vec{n}$ = normal vector to the local surface
p = pressure
p_v = vapor pressure or any other applied external pressure
$P_{\max}$ = maximum arc pressure at the arc center
$r-z$ = cylindrical coordinate system
$\vec{s}$ = local surface tangential vector
t = time
T = temperature
u = velocity in the x direction
u_w = arc voltage
v = velocity in the y direction
$\vec{V}$ = velocity vector
$\vec{V}_r$ = relative velocity vector between the liquid phase and solid phase
w = velocity in the z direction
W = melt mass evaporation rate

Greek Symbols

β_T = thermal expansion coefficient
ε = surface radiation emissivity
γ = surface tension coefficient
κ = free surface curvature
μ = dynamic viscosity
η = arc thermal efficiency
η_d = ratio of droplet thermal energy to the total arc energy
σ = Stefan–Boltzmann constant
ρ = density
σ_p = arc pressure distribution parameter
σ_q = arc heat flux distribution parameter
$\tau_{\vec{s}}$ = Marangoni shear stress

Subscripts

0 = initial condition
d = droplet
l = liquid phase
m = melting point of aluminum
s = solid phase

References

[1] Partington, E. C., 1988, "Control of Metal Transfer in Modulated Pulse M.I.G. Welding," IIW Asian Pacific Regional Welding Congress, pp. 970–988.

[2] Sunwoo, A. J., Bradley, E. L., III, and Morris, J. W., Jr., 1990, "Effects of Heat-Affected Zone Peak Temperature on the Microstructure and Properties of 2090 Al Alloy," Metall. Trans. A, **21**(10), pp. 2795–2804.

[3] Guittnerez, L. A., Neye, G., and Zschech, E., 1996, "Microstructure, Hardness Profile and Tensile Strength in Welds of AA6013 T6 Extrusions," Weld. J. (Miami, FL, U.S.), **75**(4), pp. 115s–121s.

[4] Lu, M. J., and Kou, S., 1989, "Power Inputs in Gas Metal Arc Welding of Aluminum—Part 1," Weld. J. (Miami, FL, U.S.), **68**(9), pp. 382s–388s.

[5] Kluken, A. O., and Bjorneklett, B., 1997, "A Study of Mechanical Properties for Aluminum GMA Weldments," Weld. J. (Miami, FL, U.S.), **76**(2), pp. 39–44.

[6] Ma, T., and Ouden, G., 1996, "Heat-Affected Zone Softening During Arc Welding of Al–Zn–Mg Alloys," International Journal for the Joining of Materials, **8**(3), pp. 105–110.

[7] Martukanitz, R. P., Natalie, C. A., and Knoefel, J. O., 1987, "The Weldability of an Al–Li–Cu Alloy," J. Met., **39**(11), pp. 38–42.

[8] Budnik, V. P., 1994, "Effect of the Type of Inert Gas on Pool Temperature and Fracture of the Oxide Film in Welding Aluminium," Paton Welding Journal, **6**(12), pp. 23–25.

[9] Ushio, M., and Wu, C. S., 1995, "Mathematical Modeling of Three-Dimensional Heat and Fluid Flow in a Moving Gas Metal Arc Weld Pool," Metall. Mater. Trans. B, **28B**(6), pp. 509–516.

[10] Park, H., and Rhee, S., 2001, "Analysis of Weld Geometry Considering the Transferring Droplets in Gas Metal Arc Welding," JSME Int. J., Ser. C, **44**(3), pp. 856–862.

[11] Davies, M. H., Wahab, M., and Painter, M. J., 2000, "An Investigation of the Interaction of a Molten Droplet With a Liquid Weld Pool Surface: A Computational and Experimental Approach," Weld. J. (Miami, FL, U.S.), **79**(1), pp. 18s–23s.

[12] Jaidi, J., and Dutta, P., 2001, "Modeling of Transport Phenomena in a Gas Metal Arc Welding Process," Numer. Heat Transfer, Part A, **40**, pp. 543–562.

[13] Wang, Y., and Tsai, H. L., 2001, "Impingement of Filler Droplets and Weld Pool Dynamics During Gas Metal Arc Welding Process," Int. J. Heat Mass Transfer, **44**, pp. 2067–2080.

[14] Hu, J., and Tsai, H. L., 2007, "Heat and Mass Transfer in Gas Metal Arc Welding, Part II: The Metal," Int. J. Heat Mass Transfer, **50**, pp. 808–820.

[15] Hu, J., Guo, H., and Tsai, H. L., 2008, "Weld Pool Dynamics and the Formation of Ripples in 3D Gas Metal Arc Welding," Int. J. Heat Mass Transfer, **51**, pp. 2537–2552.

[16] Praveen, P., and Yarlagadda, P. K. D. V., 2005, "Meeting Challenges in Welding of Aluminum Alloys Through Pulse Gas Metal Arc Welding," J. Mater. Process. Technol., **164–165**, pp. 1106–1112.

[17] Kothe, D. B., Mjolsness, R. C., and Torrey, M. D., 1991, "Ripple: A Computer Program for Incompressible Flows With Free Surfaces," Los Alamos National Laboratory, Report No. LA-12007-MS.

[18] Diao, Q. Z., and Tsai, H. L., 1993, "Modeling of Solute Redistribution in the Mushy Zone During Solidification of Aluminum-Copper Alloys," Metall. Trans. A, **24A**(4), pp. 963–973.

[19] Hatch, J. E., ed., 1984, *Aluminum: Properties and Physical Metallurgy*, American Society for Metals, Metals Park, OH, pp. 13–19.

[20] Zacharia, T., David, S. A., and Vitek, J. M., 1992, "Effect of Evaporation and Temperature Dependent Material Properties on Weld Pool Development," Metall. Trans. B, **22B**(2), pp. 233–241.

[21] Patankar, S. V., 1980, *Numerical Heat Transfer and Fluid Flow*, 1st ed., Hemisphere, New York, NY, pp. 41–134.

[22] 1985, *Properties and Selection: Nonferrous Alloys and Pure Metals* (Metals Handbook Vol. 2), 9th ed., American Society for Metals, Metals Park, OH, p. 113.

[23] 1985, *Metallography and Microstructures* (Metals Handbook Vol. 9), 9th ed., American Society for Metals, Metals Park, OH, pp. 352–354.

[24] Hu, J., and Tsai, H. L., 2007, "Heat and Mass Transfer in Gas Metal Arc Welding, Part I: The Arc," Int. J. Heat Mass Transfer, **50**, pp. 833–846.

[25] Hu, J., and Tsai, H. L., 2007, "Metal Transfer and Arc Plasma in Gas Metal Arc Welding," ASME J. Heat Transfer, **129**, pp. 1025–1035.

[26] Hu, J., and Tsai, H. L., 2006, "Effects of Current on Droplet Generation and Arc Plasma in Gas Metal Arc Welding," J. Appl. Phys., **100**, p. 053304.

[27] Kou, S., 1987, *Welding Metallurgy*, Wiley, New York, p. 278.

[28] Malin, V., 1995, "Study of Metallurgical Phenomena in the HAZ of 6061-T6 Aluminum Welded Joints," Weld. J. (Miami, FL, U.S.), **74**(9), pp. 305s–318s.

[29] Enjo, T., and Kuroda, T., 1982, "Microstructure in Weld Heat-Affected Zone of Al-Mg-Si Alloy," Trans. JWRI, **11**(1), pp. 61–66.

[30] Dumolt, S. D., 1983, *Metallurgical Transformations in the Heat-Affected Zone of Aluminum Alloys by Transmission Electron Microscopy*, Carnegie-Mellon University, Pittsburgh, PA.

[31] Maitland, A. H., and Ried, A., 1981, "Metallurgical Events in the Heat Affected Zone of AlMgSi Alloys," International Aluminum Welding Conference, Cleveland, OH, pp. 106–114.